nature communications

Article

https://doi.org/10.1038/s41467-025-62001-8

Dusty streaks on the Moon: fingerprints of multiphase flow instabilities

Received: 4 December 2024

Accepted: 7 July 2025

J. Sebastian Rubio[1], **Neil S. Rodrigues**[2], **Yinghe Qi**[1], **Meet Patel**[3], **Matthew T. Gorman**[1], **Miguel X. Diaz Lopez**[1], **Jesse Capecelatro**[3,4], **Paul M. Danehy**[2] & **Rui Ni**[1]

From the crewed Apollo missions to the recent Chinese Chang'e landings, the interaction between spacecraft exhaust plumes and lunar soil produces dusty clouds with high-speed particle ejection. Despite varying landing sites, remarkably stable streak patterns were observed, raising questions about their origin. We solved this puzzle by showing that these patterns were driven by Görtler instability from the curved compressed shear layer of the supersonic but surprisingly laminar jet. This instability creates vortical structures that entrain and eject particles. The number of streaks exhibits an interesting scaling with the jet pressure ratio, which can be modeled with linear instability theory and shows excellent agreement with scaled-down experiments, simulations, and actual observations in landing videos. Our findings provide a fluid physics explanation of extraterrestrial landings, highlighting the role of particle-laden flows and paving the way for future missions to optimize landing strategies and mitigate dust cloud effects on equipment and visibility.

The Moon's well-preserved surface and ancient geological features offers an unparalleled record of early Solar System history, making it a prime target for scientific exploration. Selecting optimal landing sites is crucial for both safety and scientific return. Samples from the Apollo missions on the lunar nearside revolutionized our understanding of planetary formation, lunar age, impactor population, magnetic field, and seismic activity[1–6]. Recent missions, such as the uncrewed Chang'e-5[7], filled a gap in the lunar chronology model[8,9] and revealed high water content in returned lunar samples[10,11].

In all these missions, a consistent and striking pattern of radial streaks—consisting of alternating light and dark rays extending outward from the exhaust plume's point of impingement—has been observed as the spacecraft approaches the lunar surface. Figure 1 presents images of the soil taken when the lander is just a few meters above the ground, capturing this distinct pattern. Surprisingly, despite the differences in the surface roughness, soil types, payload mass, and the nozzle designs, the streak patterns share many similarities, in particular the number of streaks shown in the images. These streaks have also been observed in terrestrial experiments conducted in preparation for the lunar landings, including those from the Apollo era[12–14], as well as in more recent studies motivated by renewed interest in space exploration[15,16].

In this work, we show that the radial streaks observed during lunar landings result from a flow instability that generates vortices in the exhaust plume, which entrain and eject surface particles into coherent patterns. The resulting concentration gradients produce distinct streaks of scattered light captured in landing footage. Through theory, experiments, and simulations, we explain the formation and scaling of these streaks, reproducing them in both terrestrial experiments and actual lunar landings.

Results

To study this landing-relevant phenomena, a canonical setup was designed, featuring a jet impinging on a granular bed that was initially flat, as shown in Fig. 2a. The Mach number at the jet exit plane is relevant for lunar lander conditions at $M_e = 5.3$, with a nozzle area ratio of 31.7. The dimensionless height, z/D_e, where z is the height from the

---

[1]Department of Mechanical Engineering, Johns Hopkins University, Baltimore, MD, USA. [2]NASA Langley Research Center, Hampton, VA, USA. [3]Department of Aerospace Engineering, University of Michigan, Ann Arbor, MI, USA. [4]Department of Mechanical Engineering, University of Michigan, Ann Arbor, MI, USA. e-mail: rui.ni@jhu.edu

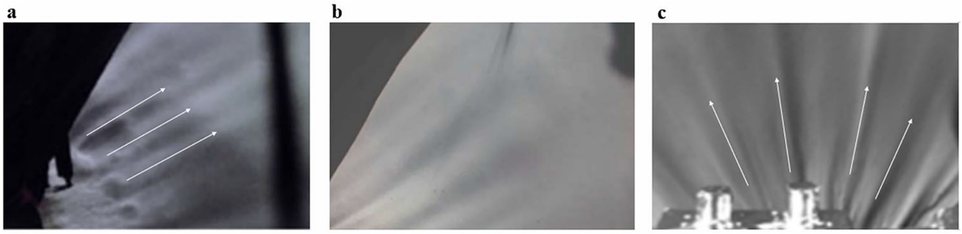

Fig. 1 | Images from different lunar landings as the spacecraft approaches the Moon's surface, generating radial ejecta streaks. **a** Apollo 12 (1969)[37], **b** Apollo 15 (1971)[36], **c** Chang'e 4 (2019)[38].

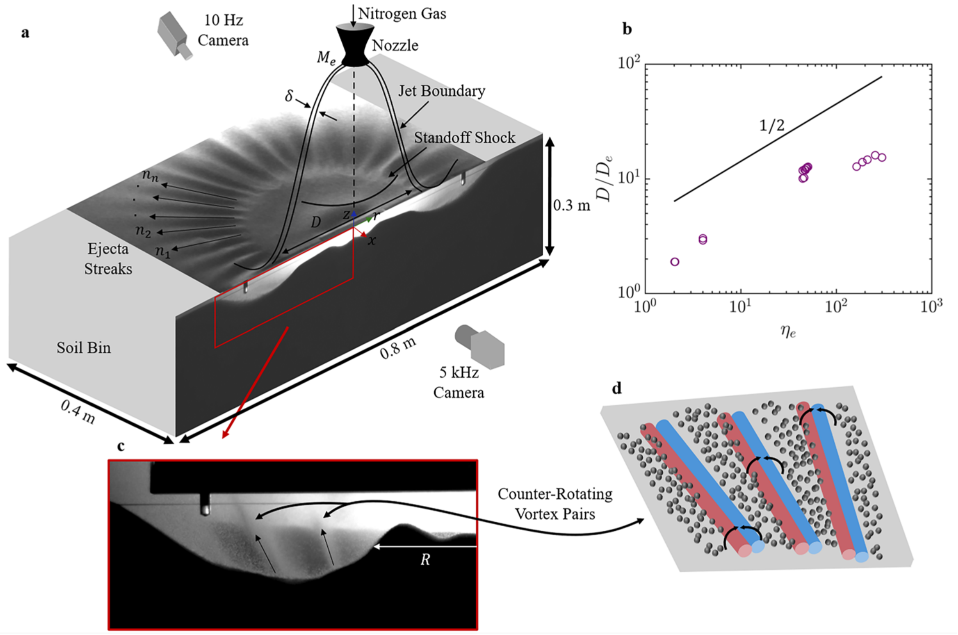

Fig. 2 | Experimental facility to study the ejecta streaks. **a** Experimental schematic of the supersonic jet impinging on a granular bed, **b** the impinging jet diameter as a function of the jet pressure ratio, **c** half-view of the front window showing the elevated ejecta streaks, and **d** schematic of counter-rotating streamwise vortices interacting with a granular bed.

nozzle to the soil surface, and D_e is the nozzle exit diameter, was varied between 3 and 13.

The nozzle was positioned downwards near a transparent side wall to allow for visualization of the cratering dynamics[17–19]. The particles were monodispersed sand with a mean diameter of $\bar{d}_p = 150\,\mu$m. A 10 Hz camera, mounted above the soil bin and pointing downward, captured the ejecta patterns. The soil bin dimensions were $80\,\text{cm}(L) \times 30\,\text{cm}(H) \times 40\,\text{cm}(W)$, providing lateral dimensions approximately 30 times the nozzle diameter to ensure that the jet expansion at impingement was not affected by the boundaries.

Reaching and maintaining low ambient pressures similar to lunar conditions posed a significant challenge. To address this, the experiment was conducted in a large walk-in vacuum chamber with a volume of $75\,\text{m}^3$, equipped with two high-capacity pumps to achieve the required low pressures. While the pumps were deactivated during gas injection, the chamber's large volume effectively minimized pressure increases during testing, ensuring the sustained low-pressure environment necessary for the experiment.

In addition to the experimental schematic, Fig. 2a illustrates the flow dynamics, overlaid with snapshots of the cratering and ejecta patterns on the r-z and r-θ planes, respectively. As the high-speed flow from the nozzle reaches the soil surface, a standoff shock forms, redirecting the flow outward along the radial r direction[12,13,20–22]. This standoff shock consists of both normal and oblique components, with the shock being parallel to the ground beneath the jet at its axis and curving further away from it[23]. This curvature leads to pressure variations beneath the shock, where the static pressure is the highest at the stagnation point and decreases radially outward[13]. At a certain radial distance, the flow accelerates to supersonic speeds as the density decreases, creating a region of maximum dynamic pressure where the surface shear stress peaks[13]. This causes erosion to initiate in an annular ring as shown in the rz plane of Fig. 2a and the zoomed-in view in Fig. 2c. The diameter (D) of the jet at impingement corresponds to the flat region below the standoff shock, where little erosion occurs within.

Outside of the impingement area, the ejecta form a periodic pattern of radial streaks. In Fig. 2c, it can be seen that the streaks appear to be lifted off the ground, suggesting that the observed patterns are not formed by surface roughness but by ejecta being preferentially concentrated in certain regions. In Fig. 2a, the ejecta streaks are visible due to more light scattered from regions with higher concentrations of particles, which can also explain the streaking phenomena observed during lunar landings as shown in Fig. 1. The total number of streaks n can be directly counted, and their wavelength λ can be defined as

$$\lambda = \frac{\pi D}{n}. \tag{1}$$

Figure 3 shows the results of n as a function of the jet pressure ratio $\eta_e = P_e/P_\infty$, defined as the ratio of the jet exit pressure P_e and the

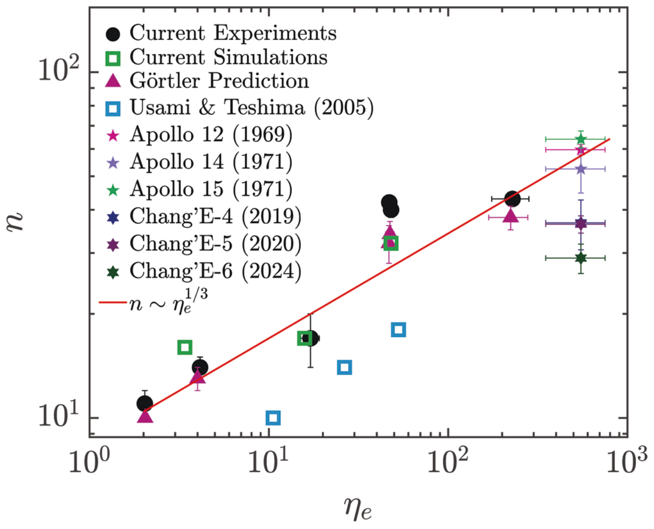

Fig. 3 | The number of streaks *n* as a function of the jet pressure ratio. The data includes current experiments and simulations, data from the literature, and estimations from the lunar landing images for the Apollo and Chang'e missions.

ambient pressure P_∞. The parameter η_e is known to dictate the structure of shocks within underexpanded jets[24]. For a lunar lander far away from the surface, η_e exceeds 10^6 due to the Moon's extremely low atmospheric pressure. However, as the lander approaches the lunar surface, the gas injection from the exhaust continues to increase the local pressure, resulting in a reduced η_e. Direct experimental measurements from the ejecta streak patterns are presented as black circles and increase with η_e. Figure 3 also shows the number of counter-rotating vortex pairs inside the compressed shear layer of a free supersonic underexpanded jet without impingement (black hollow squares)[25]. Although the number of vortex pairs is systematically lower than ours, the data follows the same trend with η_e. The smaller number may be due to the fact that the number of vortex pairs was extracted much closer to the nozzle exit without impingement. Nevertheless, the similarities between dust streaks and vortices in the compressed shear layer suggest that the dust on the surface may be entrained by a series of counter-rotating vortex lines that originate from the compressed shear layer of the jet and are retained as the jet fans out. The dust entrainment in the vortex lines is illustrated in Fig. 2d. Similar to the counter-rotating streamwise vortices observed in turbulent boundary layers[26,27], these vortices transport the heavier dust particles centrifugally to regions in between, thereby exhibiting the streak patterns. In the wall-normal direction, some particles are swept closer to the surface, while others are ejected away by those vortices. Since particles are heavier than the gas, they preferentially stay in the low momentum regions deeper in the boundary layer and eventually deposit into ridges whereas the vortex scours the surface, entraining material and leaving depressions.

Numerical simulations of underexpanded jets were performed, matching the same nozzle geometry and over a range of jet pressure ratios. They provided enhanced visualization of the flow (Supplementary Fig. 1) and supported the hypothesis that regular periodic vortical structures (Supplementary Fig. 2) originate close to the nozzle exit. The three-dimensional viscous, compressible Navier–Stokes equations were solved using high-order, energy-stable finite-difference operators on Cartesian grids. Boundary conditions were enforced at the nozzle surface via a ghost-point immersed boundary method. Additional details on the numerical scheme can be found in ref. 28 and also in the Supplementary Material.

To investigate the origin of these vortical structures, data from a corresponding single-phase experiment was used. The experiment was conducted using the same supersonic gas jet but impinging on a flat plate instead of a regolith bed, visualized with nitric oxide planar laser-induced fluorescence (NO-PLIF)[29]. The nitric oxide seed gas was at less than 1% of the overall mass flow rate and can be considered perfectly mixed within this flow configuration. Figure 4a presents a PLIF visualization for a jet with $\eta_e = 50$, where the vertical and radial coordinates are normalized by the nozzle diameter. The image intensity qualitatively corresponds to the gas density, with higher densities near the nozzle. These visualizations offer valuable insights into the rapid expansion of the jet, leading to large jet diameters. In addition, close to the jet boundary, a region between the barrel shock and jet boundary with thickness δ can be observed clearly, which we term the compressed shear layer. As η_e increases to 500 in Fig. 4d, the jet boundary becomes more diffuse, making the compressed shear layer less discernible.

Another important feature is the curvature of the jet boundary. The boundary of the supersonic underexpanded jet tends to expand and contract, leaving behind a curved jet boundary and barrel shock as shown in Fig. 4a. Simultaneously, the velocity difference between the flow inside the jet and the surrounding ambient environment generates a radial velocity gradient in the compressed shear layer. According to the Rayleigh circulation criterion[30], this flow is inherently unstable as the circulation Γ decreases with increasing radius, expressed as $\mathrm{d}\Gamma^2/\mathrm{d}r < 0$. This instability arises because the centrifugal forces within the curved compressed shear layer cannot be balanced by the pressure gradient, leading to the formation of Görtler vortices. The Görtler vortices are steady, streamwise-oriented, and counter-rotating, and they develop within the curved compressed shear layer[31,32].

To determine the existence of vortices within the compressed shear layer of the jet, the stability parameter—the Görtler number[33]—is defined as

$$G = \left(\frac{\kappa}{\varepsilon}\right)^{1/2}, \tag{2}$$

where $\kappa = \delta/\mathscr{R}$ is the ratio of the boundary layer thickness and the radius of curvature. In this definition, we replace the boundary layer thickness with the compressed shear layer thickness, as vortices form in regions of large velocity gradients. The viscous scale is defined as $\varepsilon = 1/Re_\delta$, where Re_δ is the Reynolds number based on the compressed shear layer thickness δ. The final expression for the Görtler number becomes

$$G = \left[\frac{U\delta}{\nu}\left(\frac{\delta}{\mathscr{R}}\right)\right]^{1/2}, \tag{3}$$

where U is the gas velocity just inside of the compressed shear layer, and ν is the kinematic viscosity of the fluid.

The fluid parameters in Eq. (3) are extracted from knowledge of the flow properties at the exit of the nozzle. The gas velocity is defined as $U = M_e\sqrt{\gamma R T_e}$, where $\gamma = 1.4$ is the ratio of specific heats, $R = 298.6$ J/kg · K, $M_e = 5.3$, and T_e is the temperature at the jet exit estimated from the isentropic relationship and the measured stagnation temperature. The length scales in Eq. (3) are determined directly from the single-phase PLIF images. In Fig. 4a, $\mathcal{R}$ is the reciprocal of the local curvature k computed along the z direction from the PLIF images.

Figure 4b shows the normalized radius of curvature as a function of downstream distance for $\eta_e = 50$. The radius of curvature increases to its maximum and then decreases as the flow approaches the wall. The variation of $\mathcal{R}$ with the jet pressure ratio is shown in Fig. 4c, which encompasses over two decades of variation in η_e. The same procedure was repeated for another dataset of impinging jets[34] to extract $\mathcal{R}$ at a different $M_e = 2.6$ and $\eta_e = 3.4$–18.5, which agrees with our data and follows a similar power law of $\mathcal{R} \sim \eta_e^{1/3}$ with a fitted exponent of approximately 0.33 (close to 1/3).

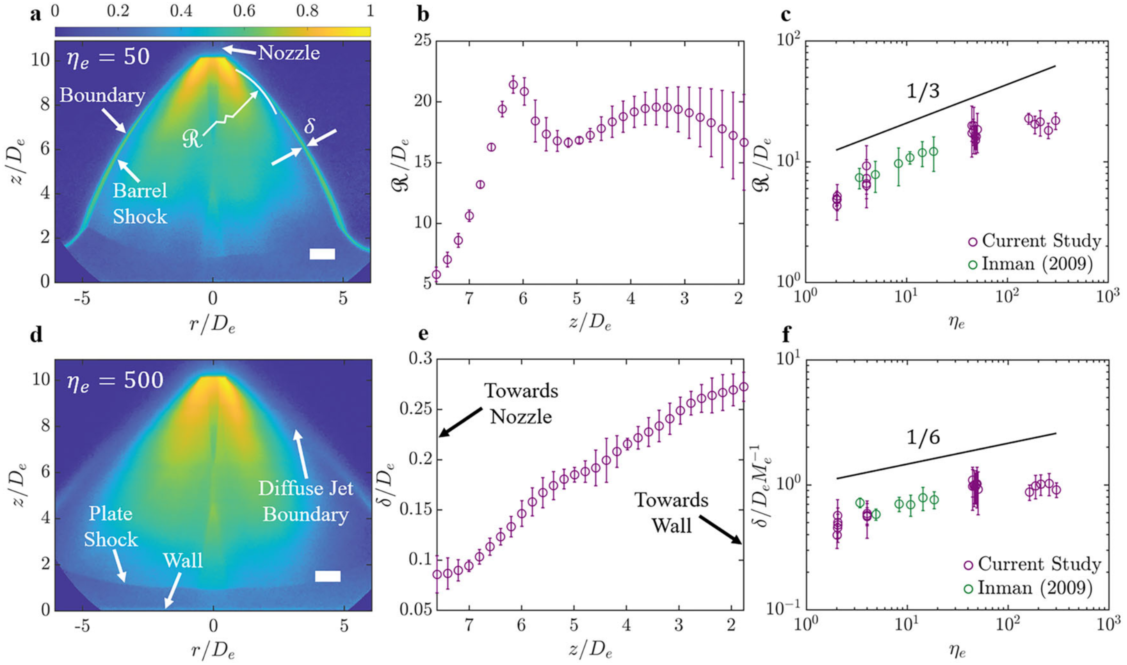

Fig. 4 | Single-phase jet profiles under varying ambient pressures. a, d Planar laser-induced fluorescence images of a Mach 5.3 jet impinging on a flat plate at $\eta_e = 50$ and $\eta_e = 500$, respectively. The scale for the color bar represents the image intensity, which qualitatively translates to the gas density. **b** The measured radius of curvature and **e** compressed shear layer thickness as a function of downstream distance for $\eta_e = 50$. **c** The radius of curvature and **f** compressed shear layer thickness as a function of the jet pressure ratio. The scale bar is 1.38 cm. Vertical bars in (**b**) and (**e**) show the standard deviation from analysis of various single-phase images at similar conditions. Vertical bars in (**c**) and (**f**) show the variation of $\mathcal{R}$ and δ in the range of z/D_e used.

The variation of δ with downstream distance is shown in Fig. 4e, showing a rapid growth up to $z/D_e = 3.5$, coinciding with the growth of the radius of curvature. After this value, δ grows at a slower rate, likely due to wall effects. The variation of the compressed shear layer thickness with η_e for current experiments, along with data from ref. 34, is shown in Fig. 4f, where δ is normalized by D_e and M_e^{-1}, with the latter, to ensure collapse of the data. Similarly, with the radius of curvature, the compressed shear layer thickness for current experiments and data from ref. 34 follow a power-law scaling of $\delta \sim \eta_e^{1/6}$ with a fitted exponent of approximately 0.167 (close to 1/6).

From the measured $\mathcal{R}$ and δ, the Görtler number can be acquired. For a Blasius boundary layer, the wave number that corresponds to the maximum instability growth rate (β) for a given Görtler number has been determined before[33]. Although the lunar lander has a large retropropulsion rocket engine resulting in a supersonic plume, the ambient density in the lunar environment is so small that the jet and its compressed shear layer is likely laminar. As a result, the relationship between β and G can still be applied here to extract the wavelength $\lambda = 2\pi\delta/\beta$ and the number of streaks by rewriting Eq. (1) as $n = \pi D/\lambda$.

The number of counter-rotating vortices computed from the Görtler instability using gas-phase data is shown as purple triangles in Fig. 3. They match exceptionally well with the direct measurements of the ejecta streaks, which provides strong support to our model.

In addition, with the scaling of the jet impingement diameter $D \sim \eta_e^{1/2}$ from Fig. 2b and $\delta \sim \eta_e^{1/6}$ from Fig. 4f, we can now formulate a prediction for the scaling of n versus η_e, which corresponds to the number of counter-rotating vortex pairs within the compressed shear layer at impingement. The scaling is shown as a red solid line in Fig. 3, which agrees with the overall trend of the experimental results.

It is important to note that, as η_e grows to larger values, the jet boundary and corresponding compressed shear layer become difficult to identify because the flow in this regime is close to being sub-continuum, and the jet boundary becomes diffusive with no clear demarcation as shown in the PLIF image in Fig. 4d. Therefore, the scaling for δ is potentially valid only up to $\eta_e \approx 500$, where the jet boundary becomes diffusive, and a defined compressed shear layer is no longer present.

Furthermore, the number of streaks that appear in the lunar landing missions was extracted directly from Fig. 1. Since most of the data only contains a small section of the plume-surface interaction region, the number of streaks are summed over a range of angles in order to estimate the total number of streaks surrounding the landing site. The estimated number ranges from 30 (Chang'e-6) to 70 (Apollo 15) with only about a factor of two in difference. Such a small difference is surprising given the wide range of variations in landing conditions, lander payload, and the rocket engine design. In addition, the number is systematically higher in Apollo missions than the Chang'e missions, which could be attributed to the fact that the camera mounted on the Apollo landers was tilted whereas the Chang'e cameras face straight to the surface. Without more information, however, it is difficult to correct for this difference.

Note that when the lander is approaching the lunar surface from afar, erosion first occurs as a cloud or haze, where no coherent dust structures are visible[35,36] because $\eta_e > 10^6$ is so large that the jet boundary is diffusive and no instability has occurred. When the lander is closer to the surface, the streaking stage begins[35], which is due to the larger local gas pressure and density from prior gas injection. As a result, the jet boundary and resulting compressed shear layer begin to emerge. Only at this moment, the streak pattern can be observed. Therefore, we approximate the effective η_e when the lander is close to the surface to be approximately $\eta_e \sim 500$. For any η_e larger than this critical number, the diffusive jet boundary will preclude any streaks from forming.

The universal nature of Görtler instabilities provides a compelling explanation for the consistency observed between scaled-down experiments on Earth and actual lunar landings. It is also noteworthy that, despite the inherently turbulent nature of supersonic flows on Earth, the supersonic flow in extraterrestrial applications could actually be laminar, which tends to generate flows at low Reynolds number but high Mach number (and high particle loadings) that have not been considered previously.

Finally, the streak patterns have not been observed in landing footage on Mars because the ambient pressure on Mars is twelve orders of magnitude higher than that on the Moon. As a result, it is likely that the rocket engine exhaust plume is both supersonic and turbulent, similar to Earth conditions. However, the heterogeneous distribution of ejecta, concentrated by turbulent instead of laminar vortical structures, still applies, but not as regular as that on the Moon. Moreover, we predict that the streak patterns should be similar for landing on the Moon and small asteroids with no atmosphere, because the pattern should only become apparent when the pressure ratio decreases to 500 or below.

Methods

The experiments were conducted at NASA Marshall Space Flight Center as part of the Plume Surface Interaction Physics Focused Ground Test 1 and 2, two experimental campaigns geared towards gaining a more comprehensive understanding on plume-surface interaction physics application to extraterrestrial landings. Two coordinated experiments were conducted in order to capture the multiphase flow and the single-phase flow behavior.

The first experiment was conducted inside a vacuum chamber with a diameter of 4.5 m and a volume of 75 m^3, capable of reaching 2.67 Pa, a lunar-relevant condition. As shown in Fig. 2a, the experimental setup is composed of a regolith bin, with the supersonic nozzle placed at the edge of the bin, which allowed for visualization of both the crater and ejecta evolution. A low-speed camera captured the particle and crater formation with a top-down view, and a high-speed camera was used to capture the evolution of the crater. Although various particle sizes and different materials were used for the experimental campaign, this study focuses on the silica sand particles with a mean diameter of 150 microns. This is due to the clear view of the ejecta streaks provided with the silica sand particles over the other materials tested.

The second experiment was conducted inside a 6-m vacuum chamber, with the matching ambient conditions as in the multiphase study. The experiment consisted of a single-phase supersonic jet, the same used as in the multiphase experiments, impinging on a rigid flat plate. To visualize the single-phase jet, planar laser-induced fluorescence (NO-PLIF) of seeded nitric oxide was used[29]. Less than 1% of the overall mass flow consisted of the seeded NO, which was premixed with heated nitrogen. A 10 Hz Nd:YAG pumped dye laser system was used to generate a tunable output of 226 nm. The laser sheet interrogated the flow at the centerline, and the fluorescence images were captured with an intensified sCMOS camera. PLIF was primarily used for flow visualization, focusing on key flow features such as the jet boundary and stagnation shocks.

Details of the simulation results can be found in the Supplementary Material. Here, we summarize some key aspects of the simulation. Numerical simulations were conducted with two nozzle geometries: a converging (sonic) nozzle, where boundary conditions were set to ensure choked flow ($M_e = 1$), corresponding to the lower range of jet pressure ratio; and a supersonic converging-diverging nozzle with an exit Mach number $M_e = 5.3$, designed to match experimental conditions. Simulations of free jets were performed to isolate and investigate the origin of streamwise streaks. These streaks were identified by visualizing the streamwise vorticity component in cross-sectional views of the jet near the nozzle exit, revealing pairs of clockwise and counterclockwise vortex structures, which were counted after the flow reached a steady state. All simulations were run on the Great Lakes high-performance computing cluster at the University of Michigan, managed by Advanced Research Computing.

Data availability

All the data supporting this work are available from the corresponding author upon request.

Code availability

Codes for simulations are available from Jesse Capecelatro (jcaps@umich.edu) upon request.

References

1. Turner, G., Cadogan, P. & Yonge, C. Apollo 17 age determinations. *Nature* **242**, 513–515 (1973).
2. Weber, R. C., Lin, P.-Y., Garnero, E. J., Williams, Q. & Lognonné, P. Seismic detection of the lunar core. *Science* **331**, 309–312 (2011).
3. Suavet, C. et al. Persistence and origin of the lunar core dynamo. *Proc. Natl. Acad. Sci. USA* **110**, 8453–8458 (2013).
4. Nichols, C. I. et al. The palaeoinclination of the ancient lunar magnetic field from an Apollo 17 basalt. *Nat. Astron.* **5**, 1216–1223 (2021).
5. Carlson, R. W. Analysis of lunar samples: implications for planet formation and evolution. *Science* **365**, 240–243 (2019).
6. Xie, M., Xiao, Z., Xu, L., Fa, W. & Xu, A. Change in the Earth–Moon impactor population at about 3.5 billion years ago. *Nat. Astron.* **5**, 128–133 (2021).
7. Liu, J. et al. Landing site selection and overview of China's lunar landing missions. *Space Sci. Rev.* **217**, 1–25 (2021).
8. Yue, Z. et al. Updated lunar cratering chronology model with the radiometric age of Chang'e-5 samples. *Nat. Astron.* **6**, 541–545 (2022).
9. Wang, B.-W. et al. Returned samples indicate volcanism on the moon 120 million years ago. *Science* **385**, 1077–1080 (2024).
10. Zhou, C. et al. Chang'e-5 samples reveal high water content in lunar minerals. *Nat. Commun.* **13**, 5336 (2022).
11. Lin, H. et al. In situ detection of water on the moon by the Chang'e-5 lander. *Sci. Adv.* **8**, eabl9174 (2022).
12. Stitt, L. E. *Interaction of Highly Underexpanded Jets with Simulated Lunar Surfaces* (National Aeronautics and Space Administration, 1961).
13. Land, N. S. & Clark, L. V. *Experimental Investigation of Jet Impingement on Surfaces of Fine Particles in a Vacuum Environment* (National Aeronautics and Space Administration, 1965).
14. Conner, D. & Land, N. *Laboratory Simulation of Lunar Surface Erosion by Rockets* (NASA-TM-X-59863, 1967).
15. Silwal, L. et al. Ejecta behavior during plume-surface interactions under rarefied atmospheric conditions. *Acta Astronaut.* **218**, 35–46 (2024).
16. Stubbs, D. C. et al. The effect of reduced ambient pressure on plume-surface interaction cratering dynamics. *AIAA J.* **63**, 1062–1077 (2025).
17. Gorman, M. T. et al. Scaling laws of plume-induced granular cratering. *PNAS Nexus* **2**, pgad300 (2023).
18. Cuesta, C. J., Davies, J., Worrall, K., Cammarano, A. & Zare-Behtash, H. Plume-surface interactions: a review of experimental work. *Acta Astronaut.* **226**, 892–912 (2025).
19. Guleria, S. D. & Patil, D. V. Experimental investigations of crater formation on granular bed subjected to an air-jet impingement. *Phys. Fluids* **32**, 053309 (2020).
20. Donaldson, C. D. & Snedeker, R. S. A study of free jet impingement. Part 1. Mean properties of free and impinging jets. *J. Fluid Mech.* **45**, 281–319 (1971).
21. Lamont, P. & Hunt, B. The impingement of underexpanded, axisymmetric jets on perpendicular and inclined flat plates. *J. Fluid Mech.* **100**, 471–511 (1980).
22. Morris, A. B., Goldstein, D. B., Varghese, P. L. & Trafton, L. M. Approach for modeling rocket plume impingement and dust dispersal on the Moon. *J. Spacecr. Rockets* **52**, 362–374 (2015).
23. Mehta, M. et al. Thruster plume surface interactions: applications for spacecraft landings on planetary bodies. *AIAA J.* **51**, 2800–2818 (2013).

24. Franquet, E., Perrier, V., Gibout, S. & Bruel, P. Free underexpanded jets in a quiescent medium: a review. *Prog. Aerosp. Sci.* **77**, 25–53 (2015).
25. Usami, M. & Teshima, K. *Three Dimensional Simulation on Deformation of Jet Boundary in an Underexpanded Axisymmetric Jet*, Vol. 762 (American Institute of Physics, 2005).
26. Robinson, S. K. Coherent motions in the turbulent boundary layer. *Annu. Rev. Fluid Mech.* **23**, 601–639 (1991).
27. Marchioli, C. & Soldati, A. Mechanisms for particle transfer and segregation in a turbulent boundary layer. *J. Fluid Mech.* **468**, 283–315 (2002).
28. Patel, M. et al. Experimental and numerical investigation of inertial particles in underexpanded jets. *J. Fluid Mech.* **1000**, A60 (2024).
29. Rodrigues, N. et al. Flow Visualization for Plume-Surface Interaction Testing within Large-Scale Vacuum Environments at Conditions Relevant to Lunar and Martian Landers. In *Joint Army-Navy-NASA-Air Force (JANNAF) meeting* (2023).
30. Rayleigh, L. On the dynamics of revolving fluids. *Proc. R. Soc. Lond. Ser. A, Containing Pap. A Math. Phys. Character* **93**, 148–154 (1917).
31. Krothapalli, A., Buzyna, G. & Lourenco, L. Streamwise vortices in an underexpanded axisymmetric jet. *Phys. Fluids A: Fluid Dyn.* **3**, 1848–1851 (1991).
32. Arnette, S., Samimy, M. & Elliott, G. On streamwise vortices in high Reynolds number supersonic axisymmetric jets. *Phys. Fluids A: Fluid Dyn.* **5**, 187–202 (1993).
33. Saric, W. S. Görtler vortices. *Annu. Rev. Fluid Mech.* **26**, 379–409 (1994).
34. Inman, J., Danehy, P., Nowak, R. & Alderfer, D. *The Effect of Impingement on Transitional Behavior in Underexpanded Jets. In 47th AIAA aerospace sciences meeting* (2009).
35. Lane, J. E., Metzger, P. T., Immer, C. D. & Li, X. in *Lagrangian Trajectory Modeling of Lunar Dust Particles* 1–9 (Earth & space 2008: Engineering, Science, Construction, and Operations in Challenging Environments, 2008).
36. Metzger, P. T., Smith, J. & Lane, J. E. Phenomenology of soil erosion due to rocket exhaust on the Moon and the Mauna Kea lunar test site. *J. Geophys. Res.: Planets* **116**, E06005 (2011).
37. Lane, J. E. & Metzger, P. T. Estimation of Apollo lunar dust transport using optical extinction measurements. *Acta Geophys.* **63**, 568–599 (2015).
38. You, J. et al. Analysis of plume–lunar surface interaction and soil erosion during the Chang'E-4 landing process. *Acta Astronaut.* **185**, 337–351 (2021).

Acknowledgements

The authors would also like to extend our gratitude to the Plume Surface Interaction Project, which was funded by the NASA Space Technology Mission Directorate (STMD) Game Changing Development (GCD) program with Samantha S. Harris from the NASA Marshall Space Flight Center (MSFC) serving as project manager and Dr. Ashley M. Korzun from the NASA Langley Research Center (LaRC) serving as principal investigator. R.N. acknowledges the support from the National Aeronautics and Space Administration under the grant number: 80NSSC19K0488. J.S.R. and M.X.D.L. receive funding from NASA Space Technology Graduate Research Opportunity under the grant number: 80NSSC20K1163 and 80NSSC22K1183, respectively; J.C. acknowledges support from the NASA Early Stage Innovations under the Grant Number: 80NSSC24K0276. The authors thank Dr. Manish Mehta for setting the initial direction of this work and wish to acknowledge the technical input on test design and direction from Dr. Jeffrey S. West, Dr. Andrew B. Weaver, and Thomas Schurtz from MSFC. The measurements reported in this article were part of a larger ground test campaign and several people from NASA are acknowledged for these efforts, including Dr. Chad J. Eberhart, Jeffrey Rayburn, Kristopher J. McDougal, Olivia K. Tyrrell, Tracy D. Reynolds, Thomas Liu, Howard A. Soohoo, and Dr. Jimmy D. Sisco.

Author contributions

J.S.R., M.T.G., M.X.D.-L., N.S.R., P.M.D., and R.N. designed the experiment; J.S.R., N.S.R., and Y.Q., analyzed the data; M.P. and J.C. performed the numerical simulations; J.S.R. and R.N. wrote the initial manuscript; all authors discussed the results and agreed on the content of the final manuscript.

Competing interests

The authors declare no competing interests.

Additional information

Supplementary information The online version contains supplementary material available at https://doi.org/10.1038/s41467-025-62001-8.

Correspondence and requests for materials should be addressed to Rui Ni.

Peer review information *Nature Communications* thanks the anonymous reviewer(s) for their contribution to the peer review of this work. A peer review file is available.